Polarization Dependence of the Optical Interband Transition
Defined by the Spatial Variation of the Valence *p*-Orbital Bloch Functions in Quantum Wires

Shinichi WATANABE*, Masahiro YOSHITA, Shyun KOSHIBA† and Hidefumi AKIYAMA

Institute for Solid State Physics, University of Tokyo, 5-1-5, Kashiwanoha, Kashiwa, Chiba 277-8581, Japan

We develop a method to express wave functions of hole states in semiconductor quantum wire (QWR) structures based on spatial variation of the valence *p*-orbital Bloch functions, to show how envelope wave functions relate to polarization-dependent interband transition. A wave function of a hole state is obtained solving the Schrödinger equation based on the 4×4 Luttinger Hamiltonian, and then recomposed by means of six bases of three *p*-orbital Bloch functions with two spin components. As a result, the hole wave function is expressed by six envelope wave functions for the six bases. Then, interband optical transition matrix elements with *x*-, *y*-, and *z*-polarizations are separately given by overlap integrals between envelope wave functions of holes for p_x, p_y, and p_z orbitals and those of electrons. We also calculate the wave functions for a modeled ridge QWR structure with mirror symmetry as well as for an asymmetric structure, and discuss the polarization dependence of the optical transition.   [DOI: 10.1143/JJAP.41.5924]

KEYWORDS: quantum wire, heterostructure, III–V semiconductor, optical property, polarization, finite element method, Luttinger Hamiltonian, transition matrix element

1. Introduction

One dimensional (1D) semiconductor quantum wire (QWR) structures[1-5] have attracted many interests these days for optical devices due to a peaked structure of 1D density of states. Especially it is predicted that QWR lasers achieve less temperature dependence[6] and lower threshold current[7] compared to conventional quantum well lasers. In order to determine and stabilize polarization of the QWR optical devices, it is important to control polarization-dependent transition matrix elements of interband transition by designing potential structures of the QWRs. Optical polarization anisotropy of the QWRs is induced by anisotropic wave functions of hole states corresponding to the potential structures. When we calculate the wave functions of the designed potential structures, it is useful to express the hole wave functions directly corresponding to the polarization-dependent transition matrix elements.

The wave functions of the hole states in the QWRs have been described in terms of admixtures of "heavy hole" ($j_z = \pm 3/2$) and "light hole" ($j_z = \pm 1/2$) states[8-13] corresponding to projections of the four-fold degenerate $J = 3/2$ states at the top of the Γ_8 bulk bands. The relative weight of each state can be obtained by solving the Schrödinger equation based on the 4×4 Luttinger Hamiltonian[14] with the envelope function approximation.[15] The polarization dependence of the interband dipole matrix element has been derived in terms of the overlap integrals between the envelope functions of electrons and holes. The optical anisotropy has been studied experimentally with photoluminescence excitation measurements by many authors,[2,16-22] and theoretical models explain those experimental results well.[19,20,23-28]

Although these calculations have been well confirmed, the correspondence between the envelope functions of the hole states and the polarization dependence of the optical transition is not so clear. The main reason is that authors

have taken $u_{j_z}^v$ ($j_z = 3/2, 1/2, -1/2, -3/2$), defined as the four degenerate Bloch functions at the top of the Γ_8 bulk bands, as the basis functions. To relate the overlap integrals between the envelope functions of the electrons and holes to the linear polarization dependence of the optical transition, it is useful to represent the hole wave functions in terms of six bases consisting of the p_x, p_y, and p_z-orbital Bloch functions with two spin components, because they separately contribute to the *x*-, *y*-, and *z*-polarized interband transitions.

McIntyre and Sham referred to this important point before,[29] but they did not describe a concrete procedure. In order to show the practical usefulness of this method, it is important to make concrete formulations corresponding to realistic potential shapes of QWRs, and numerically calculate the wave functions that can be represented as two-dimensional contour plots. Then we can have much more intuitive understanding of the overlap integrals and the transition matrix elements via the expression of a hole wave function with six bases.

In this article, we develop a method to express wave functions of hole states in semiconductor QWR structures based on spatial variation of the valence *p*-orbital Bloch functions, to show how envelope functions relate to polarization-dependent interband transition. The wave functions of the hole states are obtained solving the Schrödinger equation based on the 4×4 Luttinger Hamiltonian, and then recomposed as linear combinations of the *p*-orbital Bloch functions. The linear polarization dependence of the optical interband transition in the *x*-, *y*-, and *z*-directions can be simply discussed for each direction in terms of two components of the overlap integrals between the envelope functions of the electrons and holes. This method can be applied to any kinds of potential profile.

The structure of the article is as follows. In §2, we introduce the theoretical framework for this research. The basic Schrödinger equations and the recomposition of the wave functions are described in §2.1, and the polarization dependence of the optical interband transition is discussed in §2.2. In §2.3, we discuss the band degeneracy at the band edge due to time-reversal symmetry.

We apply our method to two kinds of potential profiles for ridge QWR structures at the band edge: a mirror-symmetric

---

*Present address: Institute of Quantum Electronics and Photonics, Swiss Federal Institute of Technology, 1015 Lausanne, Switzerland. E-mail: watanabe@dpmail.epfl.ch
†Advanced Materials Science, Faculty of Engineering, Kagawa University, 2217-20 Hayashi, Takamatsu, Kagawa 761-0396, Japan.

potential with $V(-y, z) = V(y, z)$ (§3), and an asymmetric potential (§4), and discuss the polarization dependence of the interband optical transition.

The shapes of the envelope functions depend on the quantization axis. Recently, Dupertuis *et al.* made a general and systematic theoretical analysis of the symmetry effect on the wave functions and optical polarization selection rules in QWRs.[30] They pointed out the importance of choosing an optimal quantization axis corresponding to the potential symmetry, in order to symmetrize the envelope functions for the whole Brillouin zone. They showed that the optimal quantization axis for the mirror-symmetric potential is perpendicular to the symmetric plane; namely, the y-axis when $V(-y, z) = V(y, z)$ and the z-axis when $V(y, -z) = V(y, z)$.[30] We formulate the theoretical discussions in §2 by choosing the y-quantization axis, since it is perpendicular to the mirror-symmetric plane of the potential that we discuss in §3. To apply our method to other QWRs with $V(y, -z) = V(y, z)$, it is necessary to formulate the method by choosing the z-quantization axis with appropriate Hamiltonian and base Bloch functions. The formulation in this case is described in Appendix A. We discuss the envelope functions for the asymmetric potential profile in §4 based on the y-quantization axis as used in §2.

2. Theoretical Framework

2.1 Basic equations for electronic states in quantum wires

In this section, we introduce the basic Schrödinger equation for the wave functions of electrons and holes in a QWR structure. The wave functions of the hole states are expressed as linear combinations of the p_x-, p_y- and p_z-orbital Bloch functions. We choose the [110], [$\bar{1}$10], and [001] crystal orientations as the x-, y-, and z-coordinate axes respectively, and the direction of the wire is assumed to be parallel to the x-axis. We neglect coupling between the Γ_6, Γ_8, and Γ_7 bands. We choose the y-axis as the direction of quantization, since it is perpendicular to the mirror-symmetry plane of the potential $V(-y, z) = V(y, z)$ that we discuss in §3.

The twice spin-degenerate wave functions of the electrons in QWR structures ($s = \frac{1}{2}, \sigma = \uparrow, \downarrow$) are described as a direct product of an envelope function of $\phi^c(y, z)$ and u_σ^c, defined as the cell-periodic Bloch function at the bottom of the Γ_6 bulk bands, such that

$$\Psi_\sigma^c(\boldsymbol{r}) = \frac{e^{ik_x x}}{\sqrt{L_x}} \phi^c(y, z) \cdot u_\sigma^c, \qquad (2.1)$$

where $e^{ik_x x}$ denotes a plane wave along the wire direction and L_x is the length of the wire. If the origin of the potential energy ($V = 0$) is chosen to be at the top of the Γ_8 bulk bands, the Schrödinger equation for the envelope function of the electrons can be written as

$$\left[\frac{\hbar^2}{2} \left(\frac{k_x^2}{m_e^*(y, z)} - \frac{\partial}{\partial y} \frac{1}{m_e^*(y, z)} \frac{\partial}{\partial y} - \frac{\partial}{\partial z} \frac{1}{m_e^*(y, z)} \frac{\partial}{\partial z} \right) \right.$$
$$\left. + E_g + V_e(y, z) - E_e \right] \phi^c(y, z) = 0, \qquad (2.2)$$

where $m_e^*(y, z)$ is the spatially varying effective mass of the electrons, E_g is the band gap energy, $V_e(y, z)$ is the spatially

varying confinement potential for the electrons, and E_e is the eigen quantization energy.

The wave function of the holes in QWRs cannot be represented by a single Bloch function, but by a linear combination of the four products of the envelope functions and $u_{j_y}^v$ ($j_y = \{\frac{3}{2}, \frac{1}{2}, -\frac{1}{2}, -\frac{3}{2}\}$), defined as the cell-periodic four-degenerate Bloch functions at the top of the Γ_8 bulk bands, such that

$$\Psi^v(\boldsymbol{r}) = \frac{e^{ik_x x}}{\sqrt{L_x}} \sum_{j_y} \phi_{j_y}^v(y, z) \cdot u_{j_y}^v. \qquad (2.3)$$

The Schrödinger equation for the envelope functions of the holes with four parts of $\phi_{j_y}^v$ can be represented by the 4×4 Luttinger Hamiltonian H_{Γ_8}, such that

$$[H_{\Gamma_8} + (V_h(y, z) - E_v)I] \begin{pmatrix} \phi_{3/2}^v(y, z) \\ \phi_{1/2}^v(y, z) \\ \phi_{-1/2}^v(y, z) \\ \phi_{-3/2}^v(y, z) \end{pmatrix} = 0, \qquad (2.4)$$

where $V_h(y, z)$ is the spatially varying confinement potential for the holes, E_v is the eigen quantization energy, and I is a 4×4 unit matrix. A concrete description of the Luttinger Hamiltonian and the corresponding base Bloch functions $u_{j_y}^v$ is given in Appendix A. The important point is that all the matrix elements of the Luttinger Hamiltonian are real operators, so all the envelope components of $(\phi_{3/2}^v, \phi_{1/2}^v, \phi_{-1/2}^v, \phi_{-3/2}^v)^T$ in eq. (2.4) are real functions.

To relate the overlap integrals of the envelope functions directly to the polarization dependence of the optical transition, we recompose them as linear combinations of the p-orbital Bloch functions. The wave function of the hole states can be recomposed instead of eq. (2.3) as

$$\Psi^v(\boldsymbol{r}) = \frac{e^{ik_x x}}{\sqrt{L_x}} \left[\sum_{r=x,y,z} \phi_{r,\uparrow}^v(y, z) |r \uparrow\rangle + \sum_{r=x,y,z} \phi_{r,\downarrow}^v(y, z) |r \downarrow\rangle \right],$$

where $|x\rangle$, $|y\rangle$, and $|z\rangle$ denote the cell-periodic p_x-, p_y-, and p_z-orbital Bloch functions, respectively; $|\uparrow\rangle$ and $|\downarrow\rangle$ denote spin up and down components, respectively; and

$$\phi_{x,\uparrow}^v(y, z) = i \left(\frac{1}{\sqrt{2}} \phi_{3/2}^v + \frac{1}{\sqrt{6}} \phi_{-1/2}^v \right),$$

$$\phi_{y,\uparrow}^v(y, z) = -\sqrt{\frac{2}{3}} \phi_{1/2}^v,$$

$$\phi_{z,\uparrow}^v(y, z) = \frac{1}{\sqrt{2}} \phi_{3/2}^v - \frac{1}{\sqrt{6}} \phi_{-1/2}^v,$$

$$\phi_{x,\downarrow}^v(y, z) = i \left(\frac{1}{\sqrt{2}} \phi_{-3/2}^v + \frac{1}{\sqrt{6}} \phi_{1/2}^v \right),$$

$$\phi_{y,\downarrow}^v(y, z) = -\sqrt{\frac{2}{3}} \phi_{-1/2}^v,$$

$$\phi_{z,\downarrow}^v(y, z) = -\frac{1}{\sqrt{2}} \phi_{-3/2}^v + \frac{1}{\sqrt{6}} \phi_{1/2}^v. \qquad (2.5)$$

To obtain eq. (2.5), we substitute the base Bloch functions $u_{j_y}^v$ [eq. (A·3) in Appendix A] in eq. (2.3). The wave function of the hole states can thus be described in terms of these six parts of the envelope functions by using the new base Bloch functions defined as $|r\sigma\rangle$. Note that the $\phi_{y,\sigma}^v$ and $\phi_{z,\sigma}^v$ are real

functions, while the $\phi_{x,\sigma}^{\mathrm{v}}$ are pure imaginary functions. The shapes of the six envelope functions in eq. (2.5) change when we choose a different quantization axis, since the spin parts of the base Bloch functions change.

2.2 Polarization dependence of the interband transition defined by the spatial variation of valence p-orbital Bloch functions

We next discuss the polarization dependence of the interband optical transition between the conduction and valence bands in 1D QWR structures, by using the envelope functions based on the *p*-orbital Bloch functions.

With a dipole approximation, the probability of the optical transition is proportional to $|M|^2$, defined as the square of the dipole matrix element, such that

$$|M|^2 \equiv \sum_{\sigma=\uparrow,\downarrow} \left| \langle \Psi_\sigma^{\mathrm{c}} | \boldsymbol{\epsilon} \cdot \boldsymbol{p} | \Psi^{\mathrm{v}} \rangle \right|^2$$

$$= \sum_{\sigma=\uparrow,\downarrow} \left| \sum_{r=x,y,z} I_{r,\sigma} \langle u_\sigma^{\mathrm{c}} | \boldsymbol{\epsilon} \cdot \boldsymbol{p} | r \rangle \right|^2, \qquad (2.6)$$

where $\boldsymbol{\epsilon} \equiv (\epsilon_x, \epsilon_y, \epsilon_z)$ is the polarization vector of linearly polarized light, $\boldsymbol{p} \equiv (p_x, p_y, p_z)$ is the momentum operator, and $I_{r,\sigma} \equiv \iint \phi^{\mathrm{c}}(y,z) \phi_{r,\sigma}^{\mathrm{v}}(y,z) dydz$ is the overlap integral between the envelope functions of the electrons and holes. The selection rules for the cell-periodic Bloch parts[11] are described as

$$\langle u_\sigma^{\mathrm{c}} | p_{r'} | r \rangle = \delta_{r',r} i m_0 P / \hbar, \qquad (2.7)$$

where P is the Kane matrix element.[31] We then obtain

$$|M|^2 = \left(\frac{m_0 P}{\hbar} \right)^2 \sum_{\sigma=\uparrow,\downarrow} |\boldsymbol{\epsilon} \cdot \boldsymbol{I}_\sigma|^2, \qquad (2.8)$$

where $\boldsymbol{I}_\sigma \equiv (I_{x,\sigma}, I_{y,\sigma}, I_{z,\sigma})$. $|M_r|^2$, defined as $|M|^2$ for light polarized along the *r*-direction, is given by,

$$|M_r|^2 = \left(\frac{m_0 P}{\hbar} \right)^2 \sum_{\sigma=\uparrow,\downarrow} |I_{r,\sigma}|^2, \qquad (2.9)$$

so that the sum $(\sigma = \uparrow, \downarrow)$ of $|I_{r,\sigma}|^2 \equiv |\iint \phi^{\mathrm{c}} \phi_{r,\sigma}^{\mathrm{v}} dydz|^2$ is proportional to the optical interband transition for light polarized along the *r*-direction.

$|M|^2$ in eq. (2.8) can also be written as

$$|M|^2 = \left(\frac{m_0 P}{\hbar} \right)^2 \sum_{\sigma=\uparrow,\downarrow} |\boldsymbol{\epsilon} \cdot \iint \phi^{\mathrm{c}}(y,z) \boldsymbol{\phi}_\sigma^{\mathrm{v}}(y,z) dydz|^2, \quad (2.10)$$

where $\boldsymbol{\phi}_\sigma^{\mathrm{v}} = (\phi_{x,\sigma}^{\mathrm{v}}, \phi_{y,\sigma}^{\mathrm{v}}, \phi_{z,\sigma}^{\mathrm{v}})$ and the integral is evaluated individually for each component of the vector. Comparisons between the shapes of $\phi^{\mathrm{c}}(y,z)$ and the components of $\boldsymbol{\phi}_\sigma^{\mathrm{v}}(y,z)$ can be used to directly derive the polarization dependence of the optical transition for linearly polarized light. Note that $\phi_{x,\sigma}^{\mathrm{v}}$ is the pure imaginary function, whereas $\phi_{y,\sigma}^{\mathrm{v}}$ and $\phi_{z,\sigma}^{\mathrm{v}}$ are the real functions from eq. (2.5). Thus, only the two-dimensional vector $(\phi_{y,\sigma}^{\mathrm{v}}(y,z), \phi_{z,\sigma}^{\mathrm{v}}(y,z))$, defined as the *y*- and *z*-parts of $\boldsymbol{\phi}_\sigma^{\mathrm{v}}(y,z)$, exists in real space.

2.3 Band degeneracy at the band edge

Equations (2.4) and (2.5) uniquely determine the envelope functions of the hole states in general. At the band edge $(k_x = 0)$, however, they cannot be determined uniquely

because there are degenerate eigenstates due to time-reversal symmetry.

The time-reversal symmetry causes symmetry with respect to the diagonal parts of the elements of the Luttinger Hamiltonian, leading to the two orthogonal degenerate eigenstates in eq. (2.4) as follows:

$$\begin{pmatrix} \phi_{3/2}^{\mathrm{v}}(y,z) \\ \phi_{1/2}^{\mathrm{v}}(y,z) \\ \phi_{-1/2}^{\mathrm{v}}(y,z) \\ \phi_{-3/2}^{\mathrm{v}}(y,z) \end{pmatrix} \text{and} \begin{pmatrix} \phi_{-3/2}^{\mathrm{v}}(y,z) \\ -\phi_{-1/2}^{\mathrm{v}}(y,z) \\ \phi_{1/2}^{\mathrm{v}}(y,z) \\ -\phi_{3/2}^{\mathrm{v}}(y,z) \end{pmatrix} \begin{bmatrix} u_{3/2}^{\mathrm{v}} \\ u_{1/2}^{\mathrm{v}} \\ u_{-1/2}^{\mathrm{v}} \\ u_{-3/2}^{\mathrm{v}} \end{bmatrix}, \quad (2.11)$$

where $[u_{j_y}^{\mathrm{v}}]$ describes the cell-periodic Bloch part corresponding to each row. The band degeneracy at $k_x = 0$ is independent of the shape of the confinement potential.

From the two orthogonal degenerate eigenstates, we derive two degenerate pairs, each consisting of the six parts of the recomposed envelope functions in eq. (2.5):

$$\begin{pmatrix} \phi_{x,\uparrow}^{\mathrm{v}}(y,z) \\ \phi_{y,\uparrow}^{\mathrm{v}}(y,z) \\ \phi_{z,\uparrow}^{\mathrm{v}}(y,z) \\ \phi_{x,\downarrow}^{\mathrm{v}}(y,z) \\ \phi_{y,\downarrow}^{\mathrm{v}}(y,z) \\ \phi_{z,\downarrow}^{\mathrm{v}}(y,z) \end{pmatrix} \text{and} \begin{pmatrix} \phi_{x,\downarrow}^{\mathrm{v}}(y,z) \\ -\phi_{y,\downarrow}^{\mathrm{v}}(y,z) \\ -\phi_{z,\downarrow}^{\mathrm{v}}(y,z) \\ -\phi_{x,\uparrow}^{\mathrm{v}}(y,z) \\ \phi_{y,\uparrow}^{\mathrm{v}}(y,z) \\ \phi_{z,\uparrow}^{\mathrm{v}}(y,z) \end{pmatrix} \begin{bmatrix} |x \uparrow\rangle \\ |y \uparrow\rangle \\ |z \uparrow\rangle \\ |x \downarrow\rangle \\ |y \downarrow\rangle \\ |z \downarrow\rangle \end{bmatrix}, \quad (2.12)$$

where $[|r\sigma\rangle]$ describes the cell-periodic Bloch part corresponding to each row.

Note that all the subscripts σ of the envelope functions are opposite to each other for the degenerate pairs. Since the envelope functions of the electrons corresponding to the base Bloch functions with spin up and down components are equivalent, as shown in eq. (2.1), the descriptions of $|M|^2$ become the same for one and complementary hole wave functions. The difference in sign ("+" and "−") does not affect the calculation of the transition matrix element, so it is sufficient to consider only one of the degenerate pairs in discussing the properties of the hole state at the band edge.

The degeneracy at the band edge causes the arbitrary solutions of arbitrary linear combinations of the orthogonal degenerate eigenstates. To uniquely determine the envelope function, we choose a solution to maximize the probability for the *y*- and *z*-parts of the ↑-component, defined as $\sum_{r=y,z} \iint |\phi_{r,\uparrow}^{\mathrm{v}}(y,z)|^2 dydz$, and to minimize the probability for the *y*- and *z*-parts of the ↓-component.

3. Numerical Analysis for the Mirror-Symmetric Confinement Potential

3.1 Numerical model for a ridge QWR structure

In this section, we calculate the envelope functions of the electrons $[\phi^{\mathrm{c}}(y,z)]$ and the holes $(\phi_{r,\sigma}^{\mathrm{v}}; r = x, y, z,$ and $\sigma = \uparrow, \downarrow)$ at the band edge for a modeled ridge QWR structure with mirror symmetry. Figure 1 shows a numerical model for the simplified ridge QWR structure we analyze in this section. Note that the shape of the potential profile has mirror symmetry with respect to *y*; namely, $V(-y,z) = V(y,z)$. The crystal orientation of the model is the same as both that of a real ridge QWR structure[32–34] and that we defined in the previous section.

A GaAs region embedded in $Al_{0.3}Ga_{0.7}As$ provides vertical confinement in the *z*-direction. The GaAs region
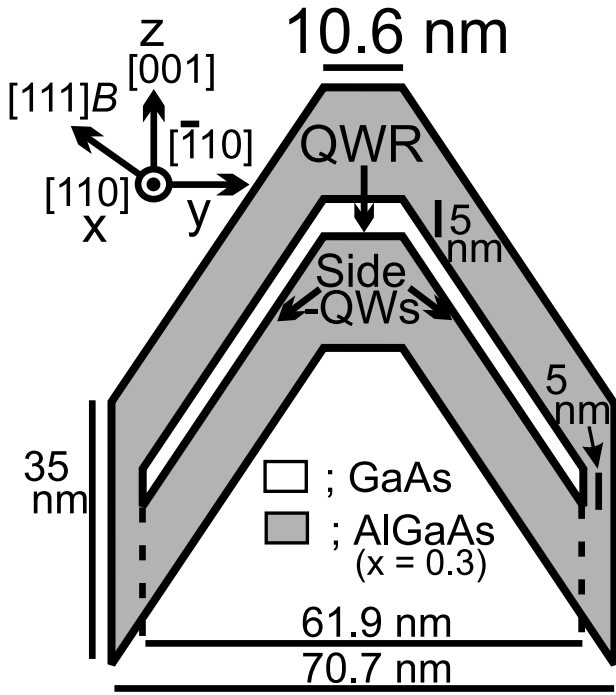
Fig. 1. A calculation model for a GaAs/Al$_{0.3}$Ga$_{0.7}$As ridge QWR structure. The GaAs region bends at two symmetric points to form a QWR and two (111)*B* side-QW structures with the same width of 5 nm along the *z*-direction. The bent GaAs region provides lateral confinement along the GaAs surface. The lateral confinement width is assumed to be 10.6 nm. We choose the *x*-, *y*-, and *z*-axes as the [110](the wire direction), [$\bar{1}$10], and [001] (the growth direction) directions respectively, corresponding to the orientations of the real ridge QWR structure. Note that the shape of the potential profile has mirror symmetry with respect *y*; namely, $V(-y, z) = V(y, z)$.

bends at two symmetric points to form a QWR and two (111)*B* side-QW structures with the same width of 5 nm along the *z*-direction. The bent GaAs region provides additional confinement; namely, lateral confinement along the GaAs layer, since the absolute values of the quantization energies in the side-QWs are higher than that in the QWR, which confines carriers in the QWR region. The carrier confinement energies due to lateral confinement, or lateral confinement energies, are defined as the differences between the quantization energies of the side-QWs and the QWR. The lateral width of the QWR region is assumed to be 10.6 nm.

The Schrödinger equations [eqs. (2.2) and (2.4)] are numerically solved by finite element analysis. A calculation region is defined as a ridge shaped structure with 70.7 nm toward *y*-direction, and 35 nm toward *z*-direction as shown in Fig. 1. We divide the calculation region rectangularly at the same interval of 0.88 nm toward *y*- and 1.25 nm toward *z*-directions. We then draw a diagonal line in each rectangular cell to divide it into two right triangular elements. The diagonals are drawn mirror-symmetrically with respect to *y* corresponding to the potential structure. As a result, 4480 right triangular elements with 2349 nodes are made in the calculation region. It is possible to divide the region at different intervals to shorten the calculation time. We divide the region at the same interval because it is easy to estimate accuracy of the results that only depends on the size of the element, and it is also easy to represent the results

Materials	GaAs	Al$_{0.3}$Ga$_{0.7}$As
Energy gap (E_{g})	1.519 eV	1.893 eV
Band offsets	68/32	
electron effective mass (m_{e})	0.0665m_0	0.0916m_0
Luttinger parameter 1 (γ_1)	6.790	5.890
Luttinger parameter 2 (γ_2)	1.924	1.716
Luttinger parameter 3 (γ_3)	2.681	2.295

as contour plots. The error of the eigen energies is estimated to be less than 5%. The material parameters for GaAs and Al$_{0.3}$Ga$_{0.7}$As are the same as those in refs. 21 and 35. and are listed in Table I.

In the case of a mirror-symmetric potential, the envelope functions are symmetrized for the whole Brillouin zone when we choose a proper quantization axis.[30] The envelope functions are symmetrized with even or odd parity in this section, since we choose a quantization axis perpendicular to the symmetric plane.[30] We call the parity "even" when the envelope function satisfies the relation $\phi(-y, z) = \phi(y, z)$, and "odd" when $\phi(-y, z) = -\phi(y, z)$. The symmetry of each recomposed envelope function is described in Appendix B.

3.2 Numerical results for the energy level and the corresponding envelope wave functions

The energy levels of the confined eigenstates of the electrons and holes at $k_x = 0$ are shown in Fig. 2. The quantization energy of electrons for the side-QWs is 134 meV higher than the Γ_6 bulk bands of GaAs, and we take this as the origin of the confinement energy level for the electrons. For holes, the quantization energy of heavy holes for the side-QWs is 30.5 meV higher than the Γ_8 bulk bands of GaAs, so we take that as the origin of the confinement energy level in this case. The quantization energy of light holes for the side-QWs is 48 meV higher than that of heavy holes.

There are two confined states for both the electrons and the holes. The lateral confinement energy of the electrons is −39.6 meV at the ground (e1) state and −3.74 meV at the second (e2) state. The lateral confinement energy of the holes is −3.45 meV at the ground (h1) state and −0.11 meV at the second (h2) state.

Figure 3 shows contour plots of the squared envelope functions defined as $|\phi^{\mathrm{c}}(y, z)|^2$ for the (a) e1 and (b) e2 states at the band edge. The notations "+" and "−" represent the sign of $\phi^{\mathrm{c}}(y, z)$. The two-dimensional confinement causes both envelope functions to be well confined at the top of the ridge structure. Note that $\phi^{\mathrm{c}}(y, z)$ for the e1 state is an even function with respect to *y*, while for the e2 state it is an odd function with a node at the top of the ridge structure. The e2 state is derived from the second subband due to the lateral confinement along the GaAs layer.

Figures 4(a)–4(f) show the six parts of the squared envelope functions for the h1 state, defined as $|\phi^{\mathrm{v}}_{r,\sigma}|^2 (r = x, y, z; \sigma = \uparrow, \downarrow)$ at the band edge. The probability of each part, defined as $\iint |\phi^{\mathrm{v}}_{r,\sigma}(y, z)|^2 dy dz$, is also shown. The notations "+" and "−" represent the sign of $\phi^{\mathrm{v}}_{r,\sigma}(y, z)$. We choose the solution to maximize the probability for the *y*- and *z*-parts of the ↑-component, as discussed in §2.3.
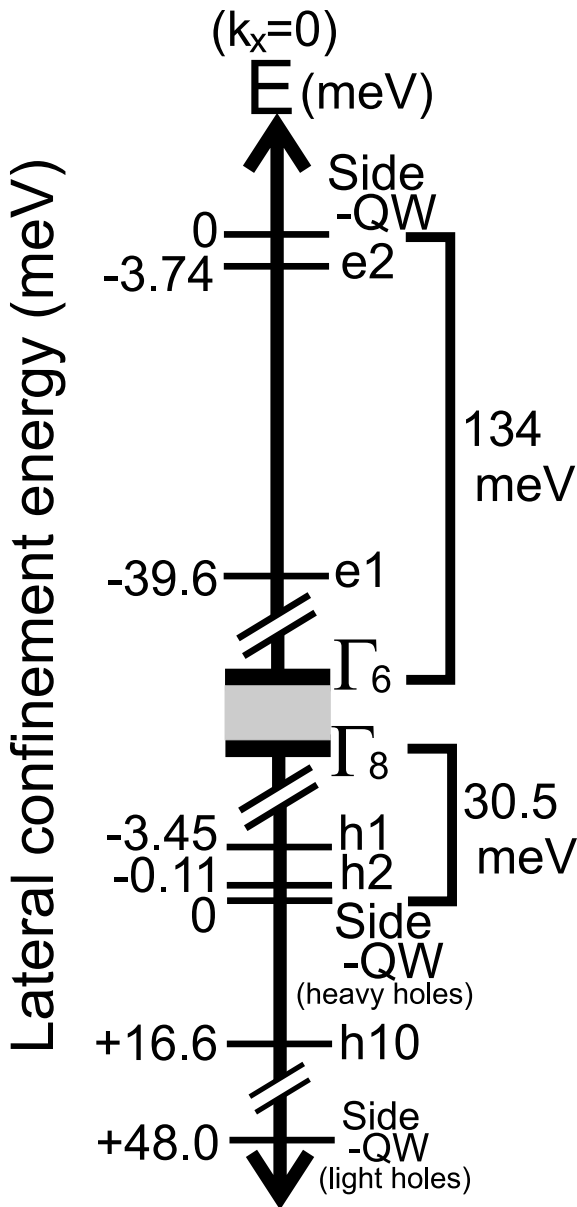
Fig. 2. The energy levels of the eigenstates of electrons and holes at $k_x = 0$ for the calculation model shown in Fig. 1. There are two confined states for both electrons and holes. The lateral confinement energies, defined as the differences in quantization energies between the side-QWs and the QWR, are -39.6 (e1), -3.74 (e2), -3.45 (h1), and -0.11 (h2) meV. The quantization energy of the h10 state is 16.6 meV higher than that of the heavy holes but 31.4 meV lower than that of the light holes for the side-QWs.
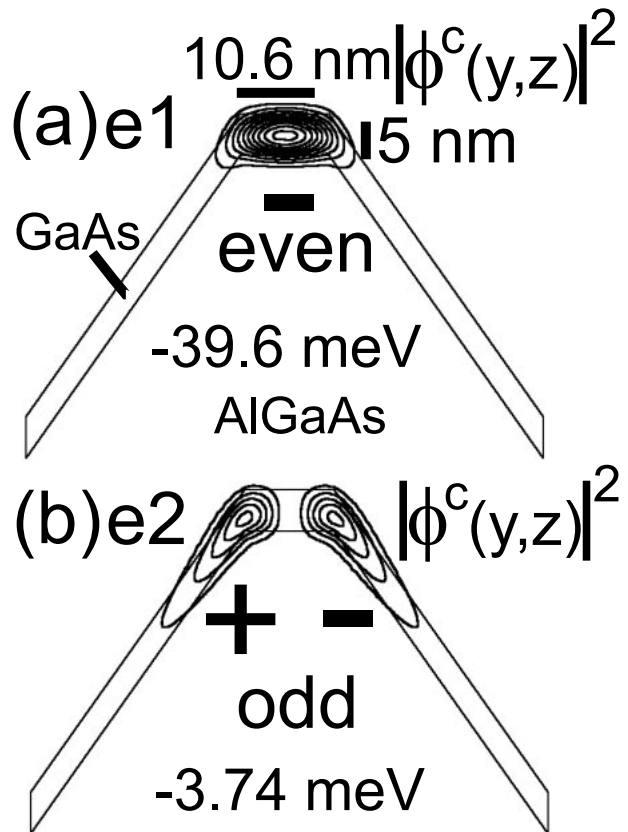

Fig. 3. Contour plots of the squared envelope functions of electrons defined as $|\phi^c(y, z)|^2$ for the (a) ground (e1) and (b) second (e2) states at the band edge $(k_x = 0)$. The lateral confinement energies are (a) -39.6 meV and (b) -3.74 meV. The wave function is normalized so that $\iint |\phi^c(y, z)|^2 dy dz = 1$ in each figure. The contour-plot lines divide the square of the envelope function into equal parts in (a), and the same interval as (a) is used in (b). The notations "+" and "−" represent the sign of $\phi^c(y, z)$. Note that the e1 state has even parity with respect to y [$\phi^c(-y, z) = \phi^c(y, z)$], while the e2 state has odd parity [$\phi^c(-y, z) = -\phi^c(y, z)$].

Figures 4(g) and 4(h) represent the spatial variation of the vectors, or the vector fields defined as $[\phi^v_{y,\uparrow}(y, z), \phi^v_{z,\uparrow}(y, z)]$ and $[\phi^v_{y,\downarrow}(y, z), \phi^v_{z,\downarrow}(y, z)]$ for the h1 state. As discussed in §2.2, only the y- and z-parts of $\boldsymbol{\phi}^v_\sigma = (\phi^v_{x,\sigma}, \phi^v_{y,\sigma}, \phi^v_{z,\sigma})$ exist in real space. The colors correspond to the lengths of the vectors, and the coordinates of the points are located at the centers of the vectors, as shown in the insets.

The parities of the envelope functions are (odd, even, odd) for the $\uparrow$-component, and (even, odd, even) for the $\downarrow$-component. The wave functions of the hole states are mixtures of even and odd states, and thus they cannot be described as either entirely even or entirely odd wave functions in general.[30]

The h1 state is dominated by (b) $\phi^v_{y,\uparrow}$, (c) $\phi^v_{z,\uparrow}$, and (d) $\phi^v_{x,\downarrow}$,

since the probabilities of these parts are much larger than those of the other three parts. The two-dimensional confinement causes (d) $\phi^v_{x,\downarrow}$ to be well confined at the top of the ridge structure, and its probability is the largest among the six parts. The properties of (b) $\phi^v_{y,\uparrow}$ and (c) $\phi^v_{z,\uparrow}$ are summarized as the vector field $(\phi^v_{y,\uparrow}, \phi^v_{z,\uparrow})$ in Fig. 4(g). The maximum vector length is at the top of the ridge structure, so that the vector field $(\phi^v_{y,\uparrow}, \phi^v_{z,\uparrow})$ is well confined at the top. Note that the directions of all the vectors are along the potential layer, which means that the y- and z-parts of the $\uparrow$-component only contains the p-orbital Bloch functions parallel to the potential layer at every local point. This is analogous to the heavy hole states of the QW structures that only contain the p-orbital Bloch functions parallel to the potential layer. So we regard the h1 state as a "heavy-hole-like" state. Lateral confinement causes this state to be well confined in the 1D QWR region.

The other three components of the h1 state with small probabilities are considered to originate from valence band mixing of the QWR structures. In particular, the vector field $(\phi^v_{y,\downarrow}, \phi^v_{z,\downarrow})$ in Fig. 4(h) shows that the components with the p-orbital Bloch function perpendicular to the potential layer mix with a minute probability.

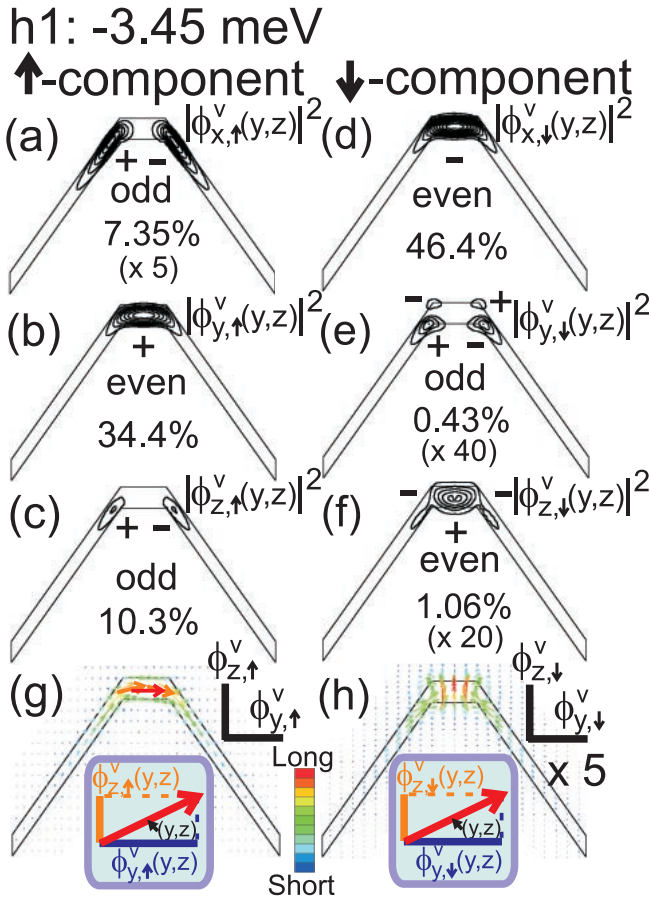Figures 5(a)–5(f) show the six parts of the squared

Fig. 4. (a)–(f) Contour plots of the six parts of the squared envelope functions for the hole ground (h1) state at the band edge. The lateral confinement energy is -3.45 meV. (a)–(c) represent the ↑-components of (a) $|\phi_{x,\uparrow}^{v}(y,z)|^2$, (b) $|\phi_{y,\uparrow}^{v}(y,z)|^2$, and (c) $|\phi_{z,\uparrow}^{v}(y,z)|^2$. (d)–(f) represent the ↓-components of (d) $|\phi_{x,\downarrow}^{v}(y,z)|^2$, (e) $|\phi_{y,\downarrow}^{v}(y,z)|^2$, and (f) $|\phi_{z,\downarrow}^{v}(y,z)|^2$. The wave function is normalized so that $\sum_{\sigma=\uparrow,\downarrow}\sum_{r=x,y,z}\iint|\phi_{r,\sigma}^{v}(y,z)|^2\,dydz=1$. The contour-plot lines divide the square of the wave function into the same intervals in (b)–(d), and in (a), (e) and (f) the intervals are (a) 5, (e) 40, and (f) 20 times shorter. The probabilities of each *p*-orbital Bloch state, defined as $\iint|\phi_{r,\sigma}^{v}(y,z)|^2\,dydz$, are (a) 7.35%, (b) 34.4%, (c) 10.3% (d) 46.4%, (e) 0.43%, and (f) 1.06%. The notations "+" and "−" represent the sign of $\phi_{r,\sigma}^{v}(y,z)$. Note that (b), (d), and (f) have even parity, while (a), (c), and (e) have odd parity. (g), (h) Spatial variations of the vectors, or the vector fields defined as $[\phi_{y,\uparrow}^{v}(y,z),\phi_{z,\uparrow}^{v}(y,z)]$ and $[\phi_{y,\downarrow}^{v}(y,z),\phi_{z,\downarrow}^{v}(y,z)]$ for the h1 state. The colors correspond to the lengths of the vectors, and the coordinates of the points are located at the centers of the vectors, as described in the insets. The lengths of the vectors in (h) are multiplied by 5 compared to (g).
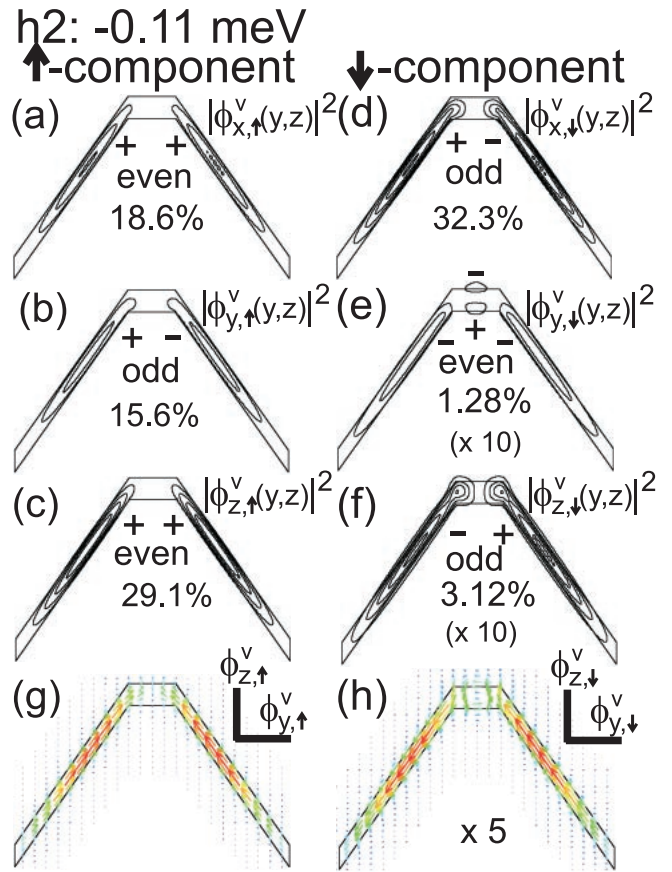
Fig. 5. (a)–(f) Contour plots of the six parts of the squared envelope functions for the h2 state at the band edge. The lateral confinement energy is -0.11 meV. The contour-plot lines divide the square of the wave function into the same intervals in (a)–(d), and the intervals are 10 times shorter in (e) and (f). The probabilities of each *p*-orbital Bloch state are also shown. (g), (h) Spatial variations of the vectors, or the vector field defined as $[\phi_{y,\uparrow}^{v}(y,z),\phi_{z,\uparrow}^{v}(y,z)]$ and $[\phi_{y,\downarrow}^{v}(y,z),\phi_{z,\downarrow}^{v}(y,z)]$ for the h2 state. The lengths of the vectors in (h) are multiplied by 5 compared to (g).

envelope functions for the h2 state at the band edge. Figures 5(g) and 5(h) represent $[\phi_{y,\uparrow}^{v}(y,z),\phi_{z,\uparrow}^{v}(y,z)]$ and $[\phi_{y,\downarrow}^{v}(y,z),\phi_{z,\downarrow}^{v}(y,z)]$ for the h2 state. The h2 state is also dominated by (b) $\phi_{y,\uparrow}^{v}$, (c) $\phi_{z,\uparrow}^{v}$, and (d) $\phi_{x,\downarrow}^{v}$, but the parity of each part is opposite to that for the h1 state. $\phi_{x,\downarrow}^{v}$ has a node at the top in Fig. 5(d). The vector with the local minimum length is also at the top in Fig. 5(g). As the directions of the vectors in Fig. 5(g) are along the potential layer, the h2 state is considered to be a second heavy-hole-like state. As for the other components, $\phi_{x,\uparrow}^{v}$ in Fig. 5(a) has two points with maximum values and contains two nodes.

The heavy-hole-like states whose quantization energies are higher than that of the heavy hole state of the side-QWs spread over the side-QW regions. But some parts of the envelope functions of the tenth (h10) state, whose quantiza-

tion energy is higher than that of the heavy hole state of the side-QWs, are again well confined at the top.

Figures 6(a)–6(f) show the six parts of the squared envelope functions for the h10 state at the band edge. The quantization energy of the h10 state is 16.6 meV higher than that of the heavy holes, but 31.4 meV lower than that of the light holes for the (111)*B* side-QWs, as shown in Fig. 2.

The six parts of the envelope functions can be divided into two groups. The envelope functions (a) $\phi_{x,\uparrow}^{v}$, (c) $\phi_{z,\uparrow}^{v}$, and (e) $\phi_{y,\downarrow}^{v}$ each have nine nodes and spread over the side-QW regions, while (b) $\phi_{y,\uparrow}^{v}$, (d) $\phi_{x,\downarrow}^{v}$, and (f) $\phi_{z,\downarrow}^{v}$ are each well confined at the top of the ridge structure. The latter group is considered to largely contain the "light-hole-like" state which is confined due to the lateral confinement. We regard the h10 state as the mixing state between the tenth heavy-hole-like state and the ground light-hole-like state.

3.3 Polarization dependence of the interband optical transition

The polarization dependence of the interband optical transition is derived from the magnitude of the overlap integral between the envelope functions of the electrons and holes. The sum ($\sigma=\uparrow,\downarrow$) of the square of the overlap integrals between ϕ^{c} in Fig. 3 and $\phi_{r,\sigma}^{v}$ in Figs. 4–6 is

h10: +16.6 meV
↑-component   ↓-component

(a) $|\phi^v_{x,\uparrow}(y,z)|^2$ (d) $|\phi^v_{x,\downarrow}(y,z)|^2$
odd — even
45.0% — 3.71%

(b) $|\phi^v_{y,\uparrow}(y,z)|^2$ (e) $|\phi^v_{y,\downarrow}(y,z)|^2$
even — odd
7.76% — 7.76%

(c) $|\phi^v_{z,\uparrow}(y,z)|^2$ (f) $|\phi^v_{z,\downarrow}(y,z)|^2$
odd — even
19.0% — 16.8%

(g) $\phi^v_{z,\uparrow}$, $\phi^v_{y,\uparrow}$ (h) $\phi^v_{z,\downarrow}$, $\phi^v_{y,\downarrow}$
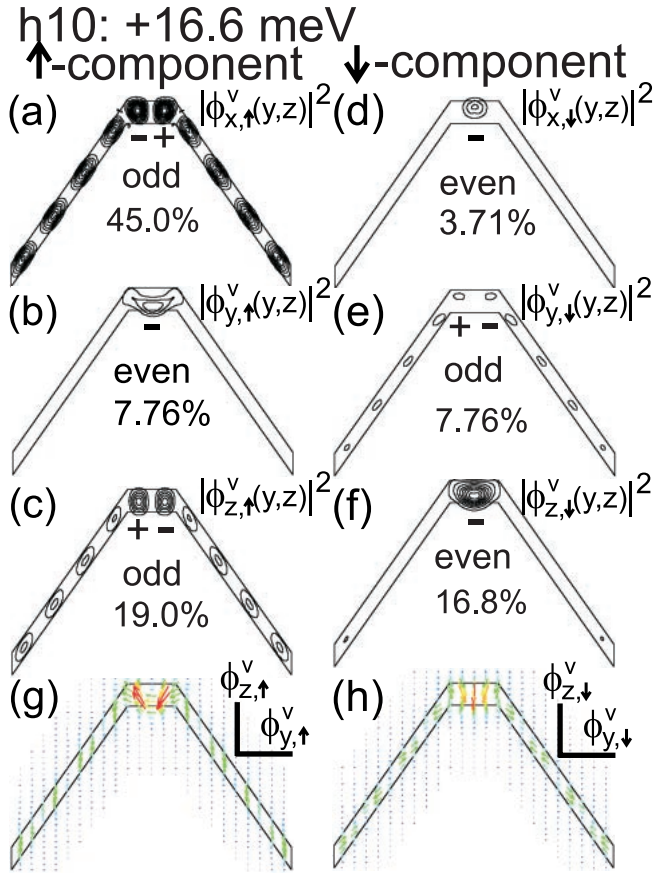
Fig. 6. (a)–(f) Contour plots of the six parts of the squared envelope functions for the h10 state at the band edge. The contour-plot lines divide the square of the wave function into the same intervals in all six figures. The probabilities of each *p*-orbital Bloch state are also shown. Note that the even components of (b), (d), and (f) are well confined at the top. (g), (h) Spatial variations of the vectors, or the vector fields defined as $[\phi^v_{y,\uparrow}(y,z), \phi^v_{z,\uparrow}(y,z)]$ and $(\phi^v_{y,\downarrow}(y,z), \phi^v_{z,\downarrow}(y,z))$ for the h10 state. The lengths of the vectors are at the same scale in each figure.

Table II. Squares of the overlap integrals and the normalized squares of the interband dipole matrix element for light polarized along the *r*-direction, for the e1–h1 and e2–h1 transitions.

	r	$|I_{r,\uparrow}|^2$	$|I_{r,\downarrow}|^2$	$(\hbar/m_0P)^2|M_r|^2$
	x	0	0.40	0.40
e1–h1	y	0.29	0	0.29
	z	0	0.0084	0.0084
	x	0.059	0	0.059
e2–h1	y	0	0.0015	0.0015
	z	0.079	0	0.079

proportional to the optical transition probability for *r*-polarized light.

We first investigate the optical transitions between the electron and h1 states; namely, the e1–h1 and e2–h1 transitions.

The upper part of Table II shows the squares of the overlap integrals of $|I_{r,\sigma}|^2 \equiv |\iint \phi^c \phi^v_{r,\sigma} dy dz|^2$ for the e1–h1 transition for all components of $r = x, y, z$, and $\sigma =\uparrow, \downarrow$. The quantity $(\hbar/m_0P)^2|M_r|^2 = |I_{r,\uparrow}|^2 + |I_{r,\downarrow}|^2$ is the normalized square of the interband dipole matrix element for light polarized along the *r*-direction.

The parity of the ↑-component of the h1 state is (odd,

even, odd) as shown in Figs. 4(a)–4(c). Thus only $|I_{y,\uparrow}|^2$ remains for the ↑-component with overlaps between the even e1 envelope function, as shown in Fig. 3(a). $|I_{y,\uparrow}|^2$ has a large value, since both ϕ^c and $\phi^v_{y,\uparrow}$ are well confined at the top of the ridge structure.

The parity of the ↓-component of the h1 state is (even, odd, even), which is opposite to that of the ↑-component. Then $|I_{x,\downarrow}|^2$ and $|I_{z,\downarrow}|^2$ remain for the ↓-component. $|I_{x,\downarrow}|^2$ also has a large value, since $\phi^v_{x,\downarrow}$ is also well confined at the top of the ridge structure. The value of $|I_{z,\downarrow}|^2$, however, is very small because the probability for $\phi^v_{z,\downarrow}$ is very small.

The sums $(\hbar/m_0P)|M_r|^2 = |I_{r,\uparrow}|^2 + |I_{r,\downarrow}|^2$ show that the optical transition for light polarized along the *x*- and *y*-directions has a large probability, while the transition for *z*-polarized light is almost forbidden. The value $(\hbar/m_0P)|M_x|^2$ (parallel to the wire) is the largest one, which is a characteristic property of 1D QWR structures. The oscillator strength is largest for *x*-polarized light, which mainly results from the probability density being the largest for the p_x components of the h1 state.

The lower part of Table II shows $|I_{r,\sigma}|^2$ and $(\hbar/m_0P)^2 |M_r|^2$ for the e2–h1 transition. The positions of the zeros for the six parts of $|I_{r,\sigma}|^2$ are opposite to those for the e1–h1 transition, since the parity of the e2 state is odd and opposite to that of the e1 state. The sums $(\hbar/m_0P)|M_r|^2$ show that the optical transition for light polarized along the *z*-direction has the largest probability. The oscillator strength is largest for the *z*-polarized light, due mainly to the probability for $\phi^v_{z,\uparrow}$ being the largest among the three odd components of the h1 state.

We next consider the optical transitions between the electron and h2 states; namely, the e1–h2 and e2–h2 transitions. Table III shows the squares of the overlap integrals of $|I_{r,\sigma}|^2$ and $(\hbar/m_0P)^2|M_r|^2$ for the e1–h2 and e2–h2 transitions. The positions of the zeros for the six parts of $|I_{r,\sigma}|^2$ are opposite to each other for the e1–h2 and e2–h2 transitions, since the parities of the e1 and e2 states are opposite. The sums $(\hbar/m_0P)|M_r|^2$ show that the polarization direction with the maximum transition probability is the *z*-direction for the e1–h2 transition. As for the e2–h2 transitions, the optical transition probabilities for light polarized along the *x*- and *y*-directions are larger.

When we compare Table III to Table II, we see that the positions of the zeros for the e1–h2 transition are opposite to those for the e1–h1 transition, because the parities of $\phi^v_{r,\sigma}(y,z)$ for the h1 state are all opposite to those for the h2 state. The squares of the interband dipole matrix elements thus depend on the shapes of both the electron and hole envelope functions. The positions of the zeros and the larger

Table III. Squares of the overlap integrals and the normalized squares of the interband dipole matrix element, for the e1–h2 and e2–h2 transitions.

	r	$|I_{r,\uparrow}|^2$	$|I_{r,\downarrow}|^2$	$(\hbar/m_0P)^2|M_r|^2$
	x	0.022	0	0.022
e1–h2	y	0	1.8×10^{-4}	1.8×10^{-4}
	z	0.026	0	0.026
	x	0	0.19	0.19
e2–h2	y	0.090	0	0.090
	z	0	0.020	0.020

Table IV. Squares of the overlap integrals and the normalized squares of the interband dipole matrix element, for the e1–h10 transition.

	r	$|I_{r,\uparrow}|^2$	$|I_{r,\downarrow}|^2$	$(\hbar/m_0P)^2|M_r|^2$
	x	0	0.014	0.014
e1–h10	y	0.049	0	0.049
	z	0	0.12	0.12

transition matrix elements are the same for the e1–h2 and e2–h1 transitions, and also for the e1–h1 and e2–h2 transitions. The values of $|M_x|^2$ and $|M_y|^2$ of the e2–h2 transition are smaller than those of the e1–h1 transition. The envelope functions for the h2 state spread over the side-QW region much more than for the e2 state, so the overlap integrals become smaller.

Table IV shows the squares of the overlap integrals of $|I_{r,\sigma}|^2$ and $(\hbar/m_0P)^2|M_r|^2$ for the e1–h10 transition. The even envelope functions of the h10 state [Figs. 6(b), 6(d), and 6(f)] are well confined at the top of the ridge structure, so the overlap integrals have relatively large values. The values of $(\hbar/m_0P)|M_r|^2$ in Table IV show that $|M_z|^2$ has the largest value.

4. Wave Functions and Optical Transition for the Asymmetric Confinement Potential

4.1 Envelope wave functions for the asymmetric confinement potential

In this section, we calculate the envelope functions for the asymmetric confinement potential of the ridge QWR structure and discuss the polarization dependence of the optical transition. The asymmetric ridge QWR structure is shown in Fig. 7(a). The confinement width of the right-hand side-QW is 25% smaller than that of the left-hand side-QW. The other parameters are the same as those shown in Fig. 1. The lateral confinement energies are defined as the differences between the quantization energies of the left-hand side-QW and the QWR.

There are two confined states for electrons and only one confined state for holes. The lateral confinement energy of the electrons is -38.8 meV at the ground (e1) state and -0.724 meV at the second (e2) state; the lateral confinement energy of the holes at the ground (h1) state is -2.77 meV.

Figure 7 shows contour plots of the squared envelope functions defined as $|\phi^c(y,z)|^2$ for the (a) e1 and (b) e2 states at the band edge. The envelope function of the e2 state is largely influenced by the asymmetric property of the potential, and it merges into the left-hand side-QW.

Figures 8(a)–8(f) show the six parts of the squared envelope functions for the h1 state at the band edge. Figures 8(g) and 8(h) represent the vector fields $[\phi^v_{y,\uparrow}(y,z), \phi^v_{z,\uparrow}(y,z)]$ and $[\phi^v_{y,\downarrow}(y,z), \phi^v_{z,\downarrow}(y,z)]$ for the h1 state. The h1 state is considered to be the heavy-hole-like state, since the dominant vector field $[\phi^v_{y,\uparrow}(y,z), \phi^v_{z,\uparrow}(y,z)]$ only contains the p-orbital Bloch functions parallel to the potential layer. The asymmetric potential causes the asymmetric profiles of the envelope functions.

4.2 Polarization dependence of the optical transition for the asymmetric confinement potential

Table V shows the squares of the overlap integrals of $|I_{r,\sigma}|^2$ ($r = x, y, z; \sigma = \uparrow, \downarrow$) and $(\hbar/m_0P)^2|M_r|^2$ for the e1–h1
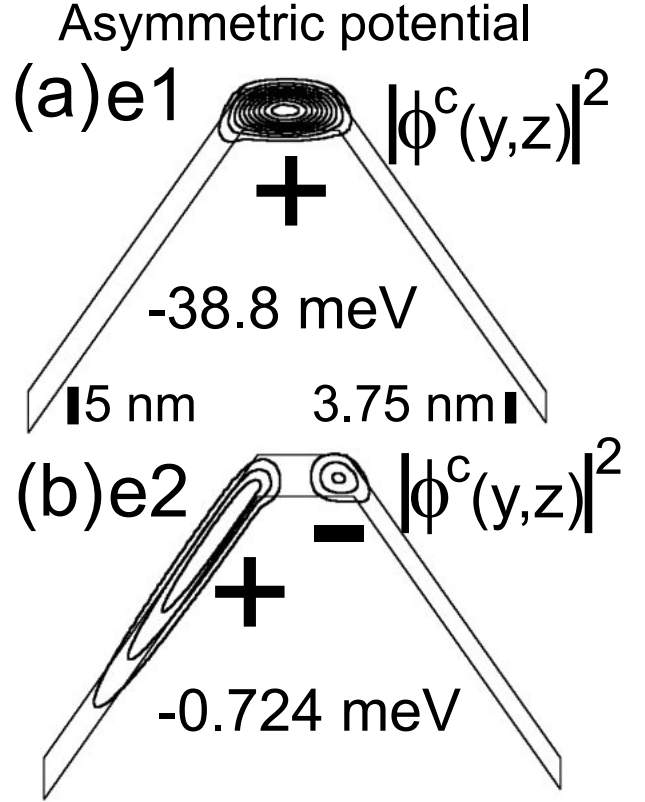

Fig. 7. Contour plots of the squared envelope functions of electrons defined as $|\phi^c(y,z)|^2$ for the (a) ground (e1), and (b) second (e2) states at the band edge for an asymmetric potential. The confinement width of the right-hand side-QW is 25% smaller than that of the left-hand side-QW. The another parameters are the same as those shown in Fig. 1. The lateral confinement energies are (a) -38.8 meV and (b) -0.724 meV for the e1 and e2 states, respectively. The wave function is normalized so that $\iint |\phi^c(y,z)|^2 dydz = 1$ in each figure. The contour-plot lines divide the square of the envelope function into the same intervals as in Fig. 3.

and e2–h1 transitions for the asymmetric potential. All the six overlap integrals of $|I_{r,\sigma}|^2$ have finite values for both transitions.

It should be noted that for the asymmetric confinement potential, the polarization vector with the maximum transition probability is not always parallel to the x-, y-, or z-directions. We now return to the general formulation of the square of the dipole matrix element in eq. (2.8). Since $\phi^v_{x,\sigma}$ and the overlap integrals of $I_{x,\sigma}$ are pure imaginary functions, we obtain

$$|M|^2 = \left(\frac{m_0P}{\hbar}\right)^2 \sum_{\sigma=\uparrow,\downarrow} [|\epsilon_x I_{x,\sigma}|^2 + (\epsilon_y I_{y,\sigma} + \epsilon_z I_{z,\sigma})^2]. \quad (4.1)$$

Note that $|M|^2$ for light polarized along the wire (the x-direction) is independent, whereas that for light polarized inside the y–z confinement plane has a cross term. When we assume the interband optical transition inside the y–z confinement plane as $\epsilon = (0, \sin\theta, \cos\theta)$, eq. (4.1) can be written as

$$|M(\theta)|^2 = \left(\frac{m_0P}{\hbar}\right)^2 \sum_{\sigma=\uparrow\downarrow} (I_{y,\sigma}\sin\theta + I_{z,\sigma}\cos\theta)^2$$

$$= \left(\frac{m_0P}{\hbar}\right)^2 \sum_{\sigma=\uparrow\downarrow} I_\sigma^2 \cos^2(\theta - \theta_\sigma), \quad (4.2)$$
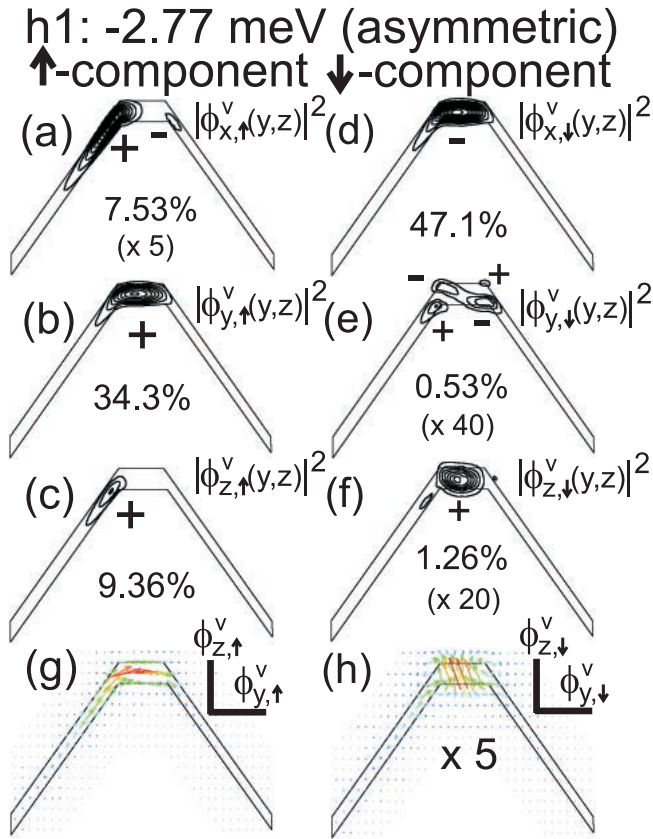
h1: -2.77 meV (asymmetric)
↑-component ↓-component

(a) $|\phi^v_{x,\uparrow}(y,z)|^2$ (d) $|\phi^v_{x,\downarrow}(y,z)|^2$

7.53%   47.1%
(× 5)

(b) $|\phi^v_{y,\uparrow}(y,z)|^2$ (e) $|\phi^v_{y,\downarrow}(y,z)|^2$

34.3%   0.53%
(× 40)

(c) $|\phi^v_{z,\uparrow}(y,z)|^2$ (f) $|\phi^v_{z,\downarrow}(y,z)|^2$

9.36%   1.26%
(× 20)

(g) $\phi^v_{z,\uparrow}$ (h) $\phi^v_{z,\downarrow}$
$\phi^v_{y,\uparrow}$ $\phi^v_{y,\downarrow}$

× 5

Fig. 8. (a)–(f) Contour plots of the six parts of the squared envelope functions for the h1 state at the band edge for the asymmetric potential. The lateral confinement energy is -2.77 meV. The contour-plot lines divide the square of the wave function into the same intervals in (b)–(d), and in (a), (e), and (f) the intervals are (a) 5, (e) 40, and (f) 20 times shorter. The probabilities of each p-orbital Bloch state are also shown. (g), (h) Spatial variations of the vectors, or the vector fields defined as $(\phi^v_{y,\uparrow}(y,z), \phi^v_{z,\uparrow}(y,z))$ and $(\phi^v_{y,\downarrow}(y,z), \phi^v_{z,\downarrow}(y,z))$ for the h1 state for the asymmetric potential. The lengths of the vectors in (h) are multiplied by 5 compared to (g).

Table V. Squares of the overlap integrals and normalized squares of the interband dipole matrix element for the e1–h1 and e2–h1 transitions for the asymmetric potential profile.

	r	$|I_{r,\uparrow}|^2$	$|I_{r,\downarrow}|^2$	$(\hbar/m_0 P)^2 |M_r|^2$
	x	0.013	0.41	0.42
	y	0.29	8.6×10^{-4}	0.29
e1–h1	z	0.0071	0.0097	0.017
	$\theta=81.4°$	0.30	2.1×10^{-4}	0.30
	$\theta=171.4°$	6.1×10^{-6}	0.010	0.010
	x	0.043	0.013	0.057
	y	0.012	9.1×10^{-4}	0.012
e2–h1	z	0.057	1.6×10^{-4}	0.057
	$\theta=24°$	0.069	5.6×10^{-4}	0.069
	$\theta=114°$	1.9×10^{-6}	5.0×10^{-4}	5.1×10^{-4}

where

$$I_\sigma = \sqrt{I^2_{y,\sigma} + I^2_{z,\sigma}},$$

$$\theta_\sigma = \arctan(I_{y,\sigma}/I_{z,\sigma}). \quad (4.3)$$

θ_σ is not equal to 0 or $\pi/2$ for the asymmetric confinement potential.

(a) e1-h1(asymmetric)
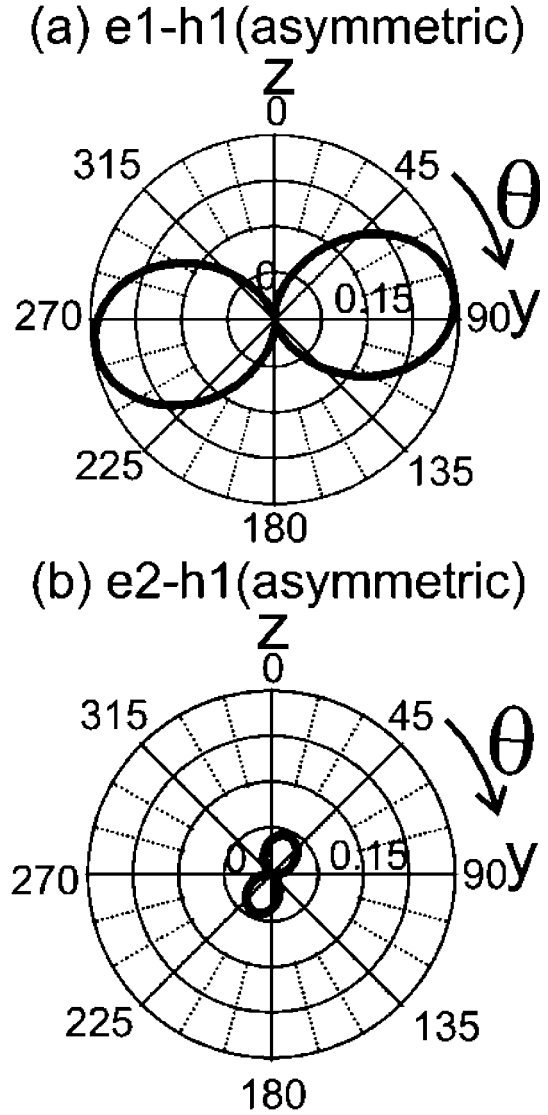
(b) e2-h1(asymmetric)

Fig. 9. Polar plots of the normalized square of the interband dipole matrix element, defined as $(\hbar/m_0 P)^2 |M(\theta)|^2$, for the (a) e1–h1 and (b) e2–h1 transitions for asymmetric potential. The largest values for light polarized inside the confinement plane are 0.30 at 81° for the e1–h1 transition and 0.068 at 24° for the e2–h1 transition.

Figure 9 shows polar plots of $(\hbar/m_0 P)^2 |M(\theta)|^2$ in eq. (4.2) for the e1–h1 and e2–h1 transitions for the asymmetric potential. The angle θ with the maximum transition probability inside the confinement plane is 81.4° for the e1–h1 transition and 24° for the e2–h1 transition. The polarization axes with the maximum transition probabilities are inclined toward the first quadrant for both transitions. Table V also shows the values of $(\hbar/m_0 P)^2 |M_r|^2$ corresponding to the directions of the polarization vector with the maximum $[(\hbar/m_0 P)^2 |M_{\text{Max}}|^2]$ and minimum $[(\hbar/m_0 P)^2 |M_{\text{Min}}|^2]$ transition probabilities inside the confinement plane for the e1–h1 and e2–h1 transitions. The degree of linear polarization inside the confinement plane, defined as $(|M_{\text{Max}}|^2 - |M_{\text{Min}}|^2)/(|M_{\text{Max}}|^2 + |M_{\text{Min}}|^2)$, is 0.94 for the e1–h1 transition and 0.99 for the e2–h1 transition. Thus the e1–h1 and e2–h1 transitions are almost linearly polarized toward 81.4 and 24°, respectively, inside the confinement plane.

To understand Fig. 9, namely, to explain the directions of

the polarization vectors with the maximum transition probabilities inside the confinement plane for the e1–h1 and e2–h1 transitions, it is useful to compare the shapes of the electron envelope functions in Fig. 7 and the dominant vector field $[\phi_{y,\uparrow}^v(y,z), \phi_{z,\uparrow}^v(y,z)]$ of the h1 state in Fig. 8(g). The envelope function of the e1 state is well confined at the top of the ridge structure, as shown in Fig. 7(a). Thus, when we calculate the e1–h1 transition matrix element, the envelope function of the e1 state largely overlaps with that of the h1 state at the top of the ridge structure. The directions of the vector field $[\phi_{y,\uparrow}^v(y,z), \phi_{z,\uparrow}^v(y,z)]$ in Fig. 8(g) almost point in the *y*-direction at the top of the ridge structure, so the transition matrix element for the e1–h1 transition is almost polarized along the *y*-direction.

On the other hand, the maximum probability density of the e2 state is at the left-hand side of the ridge structure and largely merges into the left-hand side-QW, as shown in Fig. 7(b). In this region, the directions of the vector field $[\phi_{y,\uparrow}^v(y,z), \phi_{z,\uparrow}^v(y,z)]$ of the h1 state are along the left-hand side-QW structure at 35.3° inside the confinement plane. The transition matrix element is thus polarized nearly along the left-hand side-QWs for the e2–h1 transition. As the envelope function of the e2 state also has a large probability at the right-hand side of the ridge structure, the polarization angle is smaller than 35.3°. The overlap between the e2 and h1 envelope functions is small, so the maximum transition probabilty is smaller than that for the e1–h1 transition. Thus, the spatial variation of the valeince *p*-orbital Bloch functions suggests the polarization dependence of the optical transition also in the asymmetric potentials.

We finally compare the transition matrix element along the *x*-direction to that inside the confinement *y*–*z* plane. $(\hbar/m_0 P)^2 |M_r|^2$ in Table V shows that for the e1–h1 transition the optical transition for light polarized along the *x*-direction has the largest probability. As for the e2–h1 transition, the optical transition for light polarized to 24° inside the confinement *y*–*z* plane has the largest probability, but all the values are small.

5. Conclusions

In this article, we develop a method to express wave functions of hole states in semiconductor quantum wire (QWR) structures based on spatial variation of the valence *p*-orbital Bloch functions, to show how envelope functions relate to polarization-dependent interband transition. The envelope components of the hole states in the QWRs are represented as the six parts of $\phi_{r,\sigma}^v$ ($r = x, y, z; \sigma = \uparrow, \downarrow$). The envelope functions can be summarized as two sets of vector fields defined as $\boldsymbol{\phi}_\sigma^v(y,z) \equiv (\phi_{x,\sigma}^v(y,z), \phi_{y,\sigma}^v(y,z), \phi_{z,\sigma}^v(y,z))$ $[\sigma = \uparrow, \downarrow]$. The overlap integrals between the envelope functions of the electrons and holes directly relate to the polarization dependence of the optical transition between the conduction- and valence-band states.

We have applied our method to two kinds of potential profiles for ridge QWR structures with and without mirror-symmetry at the band edge. We have also discussed the polarization dependence of the interband optical transitions.

Appendix A: Concrete Description of the Luttinger Hamiltonian

In this appendix, we describe the form of the Luttinger Hamiltonian we use in this article in choosing the *y*-quantization axis. We also describe the form of the Luttinger Hamiltonian in choosing the *z*-quantization axis.

Dupertuis *et al.* pointed out the importance of choosing an optimal quantization axis corresponding to the potential symmetry in order to symmetrize the envelope functions for the whole Brillouin zone.[30] They showed that the optimal quantization axis for the mirror-symmetric potential is perpendicular to the symmetric plane; namely, the *y*-axis when $V(-y,z) = V(y,z)$, and the *z*-axis when $V(y,-z) = V(y,z)$.[30] Figure A·1 shows three kinds of modeled QWR structures: (a) a V-groove QWR, (b) a ridge QWR, and (c) a T-shaped QWR. By choosing the [001] direction as the *z*-direction, each confinement potential $V(y,z)$ satisfies the relation $V(-y,z) = V(y,z)$ for (a) and (b), and $V(y,-z) = V(y,z)$ for (c). According to the discussions in ref. 30, we should choose the *y*-direction as the quantization axis for (a) and (b) and the *z*-direction for (c) to simplify the parity of the envelope functions for the whole Brillouin zone.

First, we describe the form of the Luttinger Hamiltonian we use in §2 in choosing the *y*-quantization axis. The Luttinger Hamiltonian H_{Γ_8} can be written using the spatially varying Luttinger parameters γ_1, γ_2, and γ_3,[36] such that

$$H_{\Gamma_8} = \begin{pmatrix} H_1 & b & c & 0 \\ b^\dagger & H_2 & 0 & c \\ c^\dagger & 0 & H_2 & -b \\ 0 & c^\dagger & -b^\dagger & H_1 \end{pmatrix}, \quad (A·1)$$

where

$$H_1 = -\frac{\hbar^2}{2m_0}\left[k_x^2 \left(\frac{2\gamma_1 - \gamma_2 + 3\gamma_3}{2} \right) \right.$$
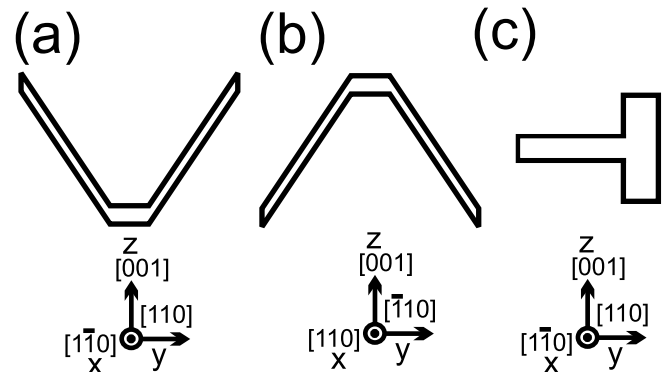

Fig. A·1.   Three kinds of modeled mirror-symmetric QWR structures, (a) a V-groove QWR, (b) a ridge QWR, and (c) a T-shaped QWR. Crystal orientations for each structure are also shown.

$$
\left. - \frac{\partial}{\partial y}\left(\frac{2\gamma_1 - \gamma_2 - 3\gamma_3}{2}\right)\frac{\partial}{\partial y} - \frac{\partial}{\partial z}(\gamma_1 + \gamma_2)\frac{\partial}{\partial z}\right],
$$

$$
H_2 = -\frac{\hbar^2}{2m_0}\left[k_x^2\left(\frac{2\gamma_1 + \gamma_2 - 3\gamma_3}{2}\right)\right.
$$
$$
\left. - \frac{\partial}{\partial y}\left(\frac{2\gamma_1 + \gamma_2 + 3\gamma_3}{2}\right)\frac{\partial}{\partial y} - \frac{\partial}{\partial z}(\gamma_1 - \gamma_2)\frac{\partial}{\partial z}\right],
$$

$$
b = -\frac{\hbar^2}{2m_0}\sqrt{3}\left[k_x\left(\gamma_2\frac{\partial}{\partial y} + \frac{\partial}{\partial y}\gamma_2\right)\right.
$$
$$
\left. + \left(\frac{\partial}{\partial y}\gamma_3\frac{\partial}{\partial z} + \frac{\partial}{\partial z}\gamma_3\frac{\partial}{\partial y}\right)\right],
$$

$$
c = \frac{\hbar^2}{2m_0}\sqrt{3}\left[\left(-\frac{\gamma_2 + \gamma_3}{2}\right)k_x^2 + \frac{\partial}{\partial y}\left(\frac{\gamma_2 - \gamma_3}{2}\right)\frac{\partial}{\partial y}\right.
$$
$$
\left. - \frac{\partial}{\partial z}\gamma_2\frac{\partial}{\partial z} - k_x\left(\gamma_3\frac{\partial}{\partial z} + \frac{\partial}{\partial z}\gamma_3\right)\right]. \tag{A·2}
$$

The base Bloch functions are written as

$$
u_{3/2}^{\rm v} = \frac{1}{\sqrt{2}}|(z + ix)\uparrow\rangle,
$$

$$
u_{1/2}^{\rm v} = \frac{1}{\sqrt{6}}|(z + ix)\downarrow\rangle - \sqrt{\frac{2}{3}}|y\uparrow\rangle,
$$

$$
u_{-1/2}^{\rm v} = -\frac{1}{\sqrt{6}}|(z - ix)\uparrow\rangle - \sqrt{\frac{2}{3}}|y\downarrow\rangle,
$$

$$
u_{-3/2}^{\rm v} = -\frac{1}{\sqrt{2}}|(z - ix)\downarrow\rangle. \tag{A·3}
$$

It should be noted that the real matrix elements of the Luttinger Hamiltonian also make all the envelope components of $(\phi_{3/2}^{\rm v}, \phi_{1/2}^{\rm v}, \phi_{-1/2}^{\rm v}, \phi_{-3/2}^{\rm v})^{\rm T}$ in eq. (2.4) real. The form of the Luttinger Hamiltonian is the same for the structures in Figs. A·1(a) and A·1(b), despite the different crystal orientations of the x- and y-axes.

Next we describe the form of the Luttinger Hamiltonian in choosing the z-quantization axis. The wave function of the hole states is written as

$$
\Psi^{\rm v}(\boldsymbol{r}) = \frac{e^{ik_xx}}{\sqrt{L_x}}\sum_{j_z}\phi_{j_z}^{\rm v'}(y, z)\cdot u_{j_z}^{\rm v'}, \tag{A·4}
$$

where

$$
u_{3/2}^{\rm v'} = \frac{1}{\sqrt{2}}|(x + iy)\uparrow'\rangle,
$$

$$
u_{1/2}^{\rm v'} = i\left[\frac{1}{\sqrt{6}}|(x + iy)\downarrow'\rangle - \sqrt{\frac{2}{3}}|z\uparrow'\rangle\right],
$$

$$
u_{-1/2}^{\rm v'} = -\frac{1}{\sqrt{6}}|(x - iy)\uparrow'\rangle - \sqrt{\frac{2}{3}}|z\downarrow'\rangle,
$$

$$
u_{-3/2}^{\rm v'} = i\left[-\frac{1}{\sqrt{2}}|(x - iy)\downarrow'\rangle\right]. \tag{A·5}
$$

The spin Bloch parts $|\uparrow'\rangle$ and $|\downarrow'\rangle$ are different from those in eq. (A·3), since we use a different quantization axis.

The p-orbital Bloch parts $|x\rangle$, $|y\rangle$, and $|z\rangle$ are the same as those in eq. (A·3). The Luttinger Hamiltonian H_{Γ_8}' is written as,

$$
H_{\Gamma_8}' = \begin{pmatrix} H_1' & b' & c' & 0 \\ b'^\dagger & H_2' & 0 & c' \\ c'^\dagger & 0 & H_2' & -b' \\ 0 & c'^\dagger & -b'^\dagger & H_1' \end{pmatrix} \tag{A·6}
$$

where

$$
H_1' = -\frac{\hbar^2}{2m_0}\left[k_x^2(\gamma_1 + \gamma_2) - \frac{\partial}{\partial y}(\gamma_1 + \gamma_2)\frac{\partial}{\partial y}\right.
$$
$$
\left. - \frac{\partial}{\partial z}(\gamma_1 - 2\gamma_2)\frac{\partial}{\partial z}\right],
$$

$$
H_2' = -\frac{\hbar^2}{2m_0}\left[k_x^2(\gamma_1 - \gamma_2) - \frac{\partial}{\partial y}(\gamma_1 - \gamma_2)\frac{\partial}{\partial y}\right.
$$
$$
\left. - \frac{\partial}{\partial z}(\gamma_1 + 2\gamma_2)\frac{\partial}{\partial z}\right],
$$

$$
b' = \frac{\hbar^2}{2m_0}\sqrt{3}\left[k_x\left(\gamma_3\frac{\partial}{\partial z} + \frac{\partial}{\partial z}\gamma_3\right)\right.
$$
$$
\left. - \left(\frac{\partial}{\partial y}\gamma_3\frac{\partial}{\partial z} + \frac{\partial}{\partial z}\gamma_3\frac{\partial}{\partial y}\right)\right],
$$

$$
c' = \frac{\hbar^2}{2m_0}\sqrt{3}\left[\gamma_3 k_x^2 + \frac{\partial}{\partial y}\gamma_3\frac{\partial}{\partial y} - k_x\left(\gamma_2\frac{\partial}{\partial y} + \frac{\partial}{\partial y}\gamma_2\right)\right]. \tag{A·7}
$$

All the matrix elements of the Luttinger Hamiltonian are real operators, so all the envelope components of $(\phi_{3/2}^{\rm v'}, \phi_{1/2}^{\rm v'}, \phi_{-1/2}^{\rm v'}, \phi_{-3/2}^{\rm v'})^{\rm T}$ are also real. Then the wave function of the hole states can be recomposed as

$$
\Psi^{\rm v}(\boldsymbol{r}) = \frac{e^{ik_xx}}{\sqrt{L_x}}\left[i\sum_{r=x,y,z}\phi_{r,\uparrow'}^{\rm v'}(y, z)|r\uparrow'\rangle\right.
$$
$$
\left. - \sum_{r=x,y,z}\phi_{r,\downarrow'}^{\rm v'}(y, z)|r\downarrow'\rangle\right],
$$

where

$$
\phi_{x,\uparrow'}^{\rm v'}(y, z) = -i\left(\frac{1}{\sqrt{2}}\phi_{3/2}^{\rm v'} - \frac{1}{\sqrt{6}}\phi_{-1/2}^{\rm v'}\right),
$$

$$
\phi_{y,\uparrow'}^{\rm v'}(y, z) = \frac{1}{\sqrt{2}}\phi_{3/2}^{\rm v'} + \frac{1}{\sqrt{6}}\phi_{-1/2}^{\rm v'},
$$

$$
\phi_{z,\uparrow'}^{\rm v'}(y, z) = -\sqrt{\frac{2}{3}}\phi_{1/2}^{\rm v'},
$$

$$
\phi_{x,\downarrow'}^{\rm v'}(y, z) = i\left(\frac{1}{\sqrt{2}}\phi_{-3/2}^{\rm v'} - \frac{1}{\sqrt{6}}\phi_{1/2}^{\rm v'}\right),
$$

$$
\phi_{y,\downarrow'}^{\rm v'}(y, z) = \frac{1}{\sqrt{2}}\phi_{-3/2}^{\rm v'} + \frac{1}{\sqrt{6}}\phi_{1/2}^{\rm v'},
$$

$$
\phi_{z,\downarrow'}^{\rm v'}(y, z) = \sqrt{\frac{2}{3}}\phi_{-1/2}^{\rm v'}. \tag{A·8}
$$

Note that the $\phi_{y,\sigma'}^{\rm v'}$ and $\phi_{z,\sigma'}^{\rm v'}$ are real functions, while the

$\phi_{x,\sigma'}^{v'}$ are pure imaginary functions. Thus only the two-dimensional vector $[\phi_{y,\sigma'}^{v'}(y,z),\phi_{z,\sigma'}^{v'}(y,z)]$ defined as the y- and z-parts of $\boldsymbol{\phi}_{\sigma'}^{v'}(y,z) = (\phi_{x,\sigma'}^{v'},\phi_{y,\sigma'}^{v'},\phi_{z,\sigma'}^{v'})$ exists in real space, which is the same as what we discuss in §2 in choosing the y-quantization axis. The shapes of these $\phi_{r,\sigma'}^{v'}$ are different from those of the $\phi_{r,\sigma}^{v}$ in eq. (2.5), since the corresponding spin Bloch parts are different.

Appendix B: Parity of the Envelope Wave Functions with Mirror-Symmetric Confinement Potential

In this appendix, we consider the parity of the recomposed envelope functions when we assume that the confinement potential has mirror symmetry $V(-y,z) = V(y,z)$ and $V(y,-z) = V(y,z)$.

When $V_e(-y,z) = V_e(y,z)$ for electrons, substituting $-y$ for y in eq. (2.2) proves that $\phi^c(-y,z)$ satisfies the same Schrödinger equation as $\phi^c(y,z)$. We then derive the relation $\phi^c(-y,z) = \pm\phi^c(y,z)$.[37] The envelope functions of electrons are thus always even or odd with respect to y when $V_e(-y,z) = V_e(y,z)$. When $V_e(y,-z) = V_e(y,z)$, the relation $\phi^c(y,-z) = \pm\phi^c(y,z)$ is thus satisfied.

As for holes, in choosing the y-quantization axis, substituting $-y$ for y in eq. (A·2) gives

$$H_1\left(-\frac{\partial}{\partial y},\frac{\partial}{\partial z}\right) = H_1\left(\frac{\partial}{\partial y},\frac{\partial}{\partial z}\right),$$

$$H_2\left(-\frac{\partial}{\partial y},\frac{\partial}{\partial z}\right) = H_2\left(\frac{\partial}{\partial y},\frac{\partial}{\partial z}\right),$$

$$b\left(-\frac{\partial}{\partial y},\frac{\partial}{\partial z}\right) = -b\left(\frac{\partial}{\partial y},\frac{\partial}{\partial z}\right),$$

$$c\left(-\frac{\partial}{\partial y},\frac{\partial}{\partial z}\right) = c\left(\frac{\partial}{\partial y},\frac{\partial}{\partial z}\right). \qquad (B·1)$$

When $V_h(-y,z) = V_h(y,z)$, these properties of the Luttinger Hamiltonian cause the following two sets of envelope functions to satisfy the same Schrödinger equation:

$$\begin{pmatrix} \phi_{3/2}^{v}(y,z) \\ \phi_{1/2}^{v}(y,z) \\ \phi_{-1/2}^{v}(y,z) \\ \phi_{-3/2}^{v}(y,z) \end{pmatrix} \text{and} \begin{pmatrix} \phi_{3/2}^{v}(-y,z) \\ -\phi_{1/2}^{v}(-y,z) \\ \phi_{-1/2}^{v}(-y,z) \\ -\phi_{-3/2}^{v}(-y,z) \end{pmatrix}. \qquad (B·2)$$

We can choose the eigen envelope functions to satisfy the relation

$$\begin{pmatrix} \phi_{3/2}^{v}(y,z) \\ \phi_{1/2}^{v}(y,z) \\ \phi_{-1/2}^{v}(y,z) \\ \phi_{-3/2}^{v}(y,z) \end{pmatrix} = \pm \begin{pmatrix} \phi_{3/2}^{v}(-y,z) \\ -\phi_{1/2}^{v}(-y,z) \\ \phi_{-1/2}^{v}(-y,z) \\ -\phi_{-3/2}^{v}(-y,z) \end{pmatrix}. \qquad (B·3)$$

Equation (B·3) then leads to the below relation for the recomposed envelope function.

$$\begin{pmatrix} \phi_{x,\uparrow}^{v}(y,z) \\ \phi_{y,\uparrow}^{v}(y,z) \\ \phi_{z,\uparrow}^{v}(y,z) \\ \phi_{x,\downarrow}^{v}(y,z) \\ \phi_{y,\downarrow}^{v}(y,z) \\ \phi_{z,\downarrow}^{v}(y,z) \end{pmatrix} = \pm \begin{pmatrix} \phi_{x,\uparrow}^{v}(-y,z) \\ -\phi_{y,\uparrow}^{v}(-y,z) \\ \phi_{z,\uparrow}^{v}(-y,z) \\ -\phi_{x,\downarrow}^{v}(-y,z) \\ \phi_{y,\downarrow}^{v}(-y,z) \\ -\phi_{z,\downarrow}^{v}(-y,z) \end{pmatrix}. \qquad (B·4)$$

Therefore, the parities of the components of $\boldsymbol{\phi}_\sigma^{v}(y,z) = (\phi_{x,\sigma}^{v}(y,z),\ \phi_{y,\sigma}^{v}(y,z),\phi_{z,\sigma}^{v}(y,z))$ become (even, odd, even) or (odd, even, odd) with respect to y, as shown in Figs. 4–6.

In choosing the z-quantization axis, substituting $-z$ for z in eq. (A·7) gives,

$$H_1'\left(\frac{\partial}{\partial y},-\frac{\partial}{\partial z}\right) = H_1'\left(\frac{\partial}{\partial y},\frac{\partial}{\partial z}\right),$$

$$H_2'\left(\frac{\partial}{\partial y},-\frac{\partial}{\partial z}\right) = H_2'\left(\frac{\partial}{\partial y},\frac{\partial}{\partial z}\right),$$

$$b'\left(\frac{\partial}{\partial y},-\frac{\partial}{\partial z}\right) = -b'\left(\frac{\partial}{\partial y},\frac{\partial}{\partial z}\right),$$

$$c'\left(\frac{\partial}{\partial y},-\frac{\partial}{\partial z}\right) = c'\left(\frac{\partial}{\partial y},\frac{\partial}{\partial z}\right). \qquad (B·5)$$

Thus, when $V_h(y,-z) = V_h(y,z)$, we can choose the eigen envelope functions to satisfy the relation

$$\begin{pmatrix} \phi_{3/2}^{v'}(y,z) \\ \phi_{1/2}^{v'}(y,z) \\ \phi_{-1/2}^{v'}(y,z) \\ \phi_{-3/2}^{v'}(y,z) \end{pmatrix} = \pm \begin{pmatrix} \phi_{3/2}^{v'}(y,-z) \\ -\phi_{1/2}^{v'}(y,-z) \\ \phi_{-1/2}^{v'}(y,-z) \\ -\phi_{-3/2}^{v'}(y,-z) \end{pmatrix}, \qquad (B·6)$$

which leads to the relation

$$\begin{pmatrix} \phi_{x,\uparrow'}^{v'}(y,z) \\ \phi_{y,\uparrow'}^{v'}(y,z) \\ \phi_{z,\uparrow'}^{v'}(y,z) \\ \phi_{x,\downarrow'}^{v'}(y,z) \\ \phi_{y,\downarrow'}^{v'}(y,z) \\ \phi_{z,\downarrow'}^{v'}(y,z) \end{pmatrix} = \pm \begin{pmatrix} \phi_{x,\uparrow'}^{v'}(y,-z) \\ \phi_{y,\uparrow'}^{v'}(y,-z) \\ -\phi_{z,\uparrow'}^{v'}(y,-z) \\ -\phi_{x,\downarrow'}^{v'}(y,-z) \\ -\phi_{y,\downarrow'}^{v'}(y,-z) \\ \phi_{z,\downarrow'}^{v'}(y,-z) \end{pmatrix} \qquad (B·7)$$

Therefore, the parities of the components of $\boldsymbol{\phi}_{\sigma'}^{v'}(y,z) = (\phi_{x,\sigma'}^{v'}(y,z),\ \phi_{y,\sigma'}^{v'}(y,z),\ \phi_{z,\sigma'}^{v'}(y,z))$ become (even, even, odd) or (odd, odd, even) with respect to z.

1) P. M. Petroff, A. C. Gossard, R. A. Logan and W. Wiegmann: Appl. Phys. Lett. **41** (1982) 635.
2) M. Tsuchiya, J. M. Gaines, R. H. Yan, R. J. Simes, P. O. Holtz, L. A. Coldren and P. M. Petroff: Phys. Rev. Lett. **62** (1989) 466.
3) E. Kapon, D. M. Hwang and R. Bhat: Phys. Rev. Lett. **63** (1989) 430.
4) A. R. Goñi, L. N. Pfeiffer, K. W. West, A. Pinczuk, H. U. Baranger and H. L. Stormer: Appl. Phys. Lett. **61** (1992) 1956.
5) S. Koshiba, H. Noge, H. Akiyama, T. Inoshita, Y. Nakamura, A. Shimizu, Y. Nagamune, M. Tsuchiya, H. Kano and H. Sakaki: Appl. Phys. Lett. **64** (1994) 363.
6) Y. Arakawa and H. Sakaki: Appl. Phys. Lett. **40** (1982) 939.
7) M. Asada, Y. Miyamoto and Y. Suemune: Jpn. J. Appl. Phys. **24** (1985) L95.
8) I. Suemune and L. A. Coldren: IEEE J. Quantum Electron. **24** (1988) 1778.
9) U. Bockelmann and G. Bastard: Europhys. Lett. **15** (1991) 215.
10) P. C. Sercel and K. J. Vahala: Phys. Rev. B **44** (1991) 5681.
11) U. Bockelmann and G. Bastard: Phys. Rev. B **45** (1992) 1688.
12) W. Langbein, H. Gislason and J. M. Hvam: Phys. Rev. B **54** (1996) 14595.
13) M. Ogawa, T. Kunimasa, T. Ito and T. Miyoshi: J. Appl. Phys. **84** (1998) 3242.
14) J. M. Luttinger and W. Kohn: Phys. Rev. **97** (1955) 869.
15) G. Bastard: *Wave Mechanics Applied to Semiconductor Heterostructures* (Les Editions de Physique, Les Ulis, 1988).
16) M. Tanaka and H. Sakaki: Appl. Phys. Lett. **54** (1989) 1326.

17) H. Akiyama, T. Someya and H. Sakaki: Phys. Rev. B **53** (1996) R4229.

18) H. Akiyama, T. Someya and H. Sakaki: Phys. Rev. B **53** (1996) R10520.

19) T. Sogawa, H. Ando, S. Ando and H. Kanbe: Phys. Rev. B **56** (1997) 1958.

20) F. Vouilloz, D. Y. Oberli, M. A. Dupertuis, A. Gustafsson, F. Reinhardt and E. Kapon: Phys. Rev. Lett. **78** (1997) 1580.

21) F. Vouilloz, D. Y. Oberli, M. A. Dupertuis, A. Gustafsson, F. Reinhardt and E. Kapon: Phys. Rev. B **57** (1998) 12378.

22) E. Martinet, M. A. Dupertuis, L. Sirigu, D. Y. Oberli, A. Rudra, K. Leifer and E. Kapon: Phys. Status Solidi A **178** (2000) 233.

23) D. S. Citrin and Y. C. Chang: Phys. Rev. B **43** (1991) 11703.

24) A. A. Yamaguchi, K. Nishi and A. Usui: Jpn. J. Appl. Phys. **33** (1994) L912.

25) G. Goldoni, F. Rossi, E. Molinari and A. Fasolino: Phys. Rev. B **55** (1997) 7110.

26) T. Sogawa, H. Ando, S. Ando and H. Kanbe: Phys. Rev. B **58** (1998) 15652.

27) M. A. Dupertuis: Phys. Status Solidi A **178** (2000) 221.

28) A. Siarkos and E. Runge: Phys. Rev. B **61** (2000) 16854.

29) C. R. McIntyre and L. J. Sham: Phys. Rev. B **45** (1992) 9443.

30) M. A. Dupertuis, E. Martinet, D. Y. Oberli and E. Kapon: Europhys. Lett. **52** (2000) 420.

31) E. O. Kane: J. Phys. Chem. Solids **1** (1957) 249.

32) S. Watanabe, S. Koshiba, M. Yoshita, H. Sakaki, M. Baba and H. Akiyama: Appl. Phys. Lett. **73** (1998) 511.

33) S. Koshiba, S. Watanabe, Y. Nakamura, M. Yamauchi, M. Yoshita, M. Baba, H. Akiyama and H. Sakaki: J. Cryst. Growth **201/202** (1999) 810.

34) S. Watanabe, S. Koshiba, M. Yoshita, H. Sakaki, M. Baba and H. Akiyama: Appl. Phys. Lett. **75** (1999) 2190.

35) L. W. Molenkamp, R. Eppenga, G. W. 't Hooft, P. Dawson, C. T. Foxon and K. J. Moore: Phys. Rev. B **38** (1988) 4314.

36) J. M. Luttinger: Phys. Rev. **102** (1956) 1030.

37) L. I. Schiff: *Quantum Mechanics* (McGraw-Hill, New York, 1968) 3rd ed., Chap. 2, Sect. 9.